Multifluid Simulation of Solar Chromospheric Turbulence and Heating Due to Thermal Farley–Buneman Instability

Samuel Evans[1] , Meers Oppenheim[1] , Juan Martínez-Sykora[2,3,4,5] , Yakov Dimant[1] , and Richard Xiao[1]
[1] Boston University Center for Space Physics, 725 Commonwealth Ave., Boston, MA 02215, USA
[2] Lockheed Martin Solar & Astrophysics Laboratory, 3251 Hanover St., Palo Alto, CA 94304, USA
[3] Bay Area Environmental Research Institute, NASA Research Park, Moffett Field, CA 94035, USA
[4] Rosseland Centre for Solar Physics, University of Oslo, P.O. Box 1029 Blindern, NO-0315 Oslo, Norway
[5] Institute of Theoretical Astrophysics, University of Oslo, P.O. Box 1029 Blindern, NO-0315 Oslo, Norway
Received 2022 November 11; revised 2023 March 9; accepted 2023 March 18; published 2023 May 30

Abstract

Models fail to reproduce observations of the coldest parts of the Sun's atmosphere, where interactions between multiple ionized and neutral species prevent an accurate MHD representation. This paper argues that a meter-scale electrostatic plasma instability develops in these regions and causes heating. We refer to this instability as the Thermal Farley–Buneman Instability (TFBI). Using parameters from a 2.5D radiative MHD Bifrost simulation, we show that the TFBI develops in many of the colder regions in the chromosphere. This paper also presents the first multifluid simulation of the TFBI and validates this new result by demonstrating close agreement with theory during the linear regime. The simulation eventually develops turbulence, and we characterize the resulting wave-driven heating, plasma transport, and turbulent motions. These results all contend that the effects of the TFBI contribute to the discrepancies between solar observations and radiative MHD models.

Unified Astronomy Thesaurus concepts: Solar chromosphere (1479); Solar chromospheric heating (1987); Plasma physics (2089); Astronomical simulations (1857)

Supporting material: animation

1. Introduction

The chromosphere is the complex interface region between the photosphere and the million-degree corona. For solar modeling, it is crucial to understand the chromosphere, since all energy transfer from the surface of the Sun to the corona must pass through this intermediary region. The chromosphere presents a modeling challenge, as it spans many parameter regimes, microphysics may play an important role, and the assumptions of MHD break down. Over the last few decades, large improvements have been made with radiative (M)HD models, which capture a large variety of chromospheric dynamics such as magnetoacoustic shocks (see, e.g., Carlsson & Stein 1992, 1995, 2002; Wedemeyer et al. 2004; Carlsson 2007), spicules (Hansteen et al. 2007; Martínez-Sykora et al. 2017), and flux emergence (Cheung & Isobe 2014). Some models have been further improved to include the effects of ion–neutral interactions (Leake et al. 2014; Martínez-Sykora et al. 2015; Ballester et al. 2018, and references therein) and nonequilibrium ionization (Leenaarts et al. 2007; Golding et al. 2014; Przybylski et al. 2022).

However, comparisons between chromospheric observables and synthesis from those models reveal large discrepancies in some areas. The observed profiles, such as Mg II h and k from IRIS (De Pontieu et al. 2014), are typically wider than the corresponding profiles synthesized from simulations (Carlsson et al. 2019). Also, radiative MHD (rMHD) models predict excessively cold chromospheres; simulation temperatures reach down to 2000 K, even though recent inversions of observations suggest temperatures of at least 3000 K (da Silva Santos et al.

2020). Semiempirical models suggest a temperature minimum closer to 4000 K (Fontenla et al. 2009), although they do not include dynamics or associated thermal properties. Comparing observations from IRIS and the Atacama Large Millimeter/submillimeter Array to recent single-fluid rMHD models, which include ion–neutral interactions and nonequilibrium effects, also indicates that the spicules are up to a few thousand degrees colder in the models from simulations (Chintzoglou et al. 2021). These issues might be alleviated by including the heating and turbulent effects of small-scale plasma instabilities, which are missing from such models.

Fontenla (2005) and Fontenla et al. (2008) originally suggested that the Farley–Buneman (FB) instability can lead to heating in the chromosphere. They argued that convective motions of neutral gas drag the mostly collisionally demagnetized ions across the solar magnetic field while the electron motion remains primarily tied to the magnetic field lines. This causes the development of currents and electrostatic waves that lead to instability, as described in Dimant & Sudan (1995). The work by Fontenla (2005) and Fontenla et al. (2008) treats the FB instability appropriately for the ionosphere, where it was originally discovered, but neglects crucial terms that become relevant in the chromosphere. Madsen et al. (2014) include some such terms by treating the instability with a multifluid model yet neglects proton magnetization; Fletcher et al. (2018) shows that ion magnetization effects reduce the prevalence of the instability in the chromosphere.

By simulating the instability using a kinetic particle-in-cell (PIC) code, Oppenheim et al. (2020) discovered that temperature perturbations significantly affect instability properties under chromospheric parameters. They improved the theory to include these thermal effects, predicting the new instability that we refer to as the Thermal Farley–Buneman Instability (TFBI). Oppenheim et al. (2020) also applied a simplified form of the

theory to solar atmospheric simulator output to predict that the instability occurs throughout the chromosphere; we validate this result by pairing the full linear theory with output from an improved simulation that incorporates more physics. Dimant et al. (2022) further studied the linear theory of this instability in different limiting cases and determined that a multifluid model may be sufficient to reproduce the TFBI for chromospheric parameters.

The TFBI may occur in regions other than the solar chromosphere as well. It could appear in other stellar atmospheres and likely appears in various planetary ionospheres, including Earth's ionosphere, where thermal and FB instabilities have been studied in the past (see, e.g., Dimant & Sudan 1995; Dimant & Oppenheim 2004; Kagan & St.-Maurice 2004). It may affect the dynamics in molecular clouds and heat transfer in accretion disks. Any partially ionized plasma having sufficiently strong flows across magnetic field lines, along with the appropriate fluid densities and temperatures, would produce the TFBI.

To study the TFBI in the Sun's chromosphere, we utilize the new multifluid code, Ebysus (Martínez-Sykora et al. 2020). Ebysus treats each ionized level of each atomic species as a separate fluid, with the ability to handle any number of fluids in the same simulation. Using Ebysus, we simulate the multifluid TFBI in a fluid-model code for the first time. We demonstrate a close agreement between this simulation and linear theory and show that the nonlinear effects from this simulation produce heating, transport, and turbulent motions. Such effects might be responsible for heating, altering conductivities, and broadening spectral lines in the chromosphere while also being absent from state-of-the-art models of this region. The ability to produce this instability in a fluid-model code enables studies at larger scales and across more chromospheric parameter regimes than what is possible with kinetic codes alone.

The remainder of this paper is structured as follows. Section 2 discusses the instability theory and simulation setup. Section 3.1 details our prediction that the multifluid TFBI occurs throughout the Sun's chromosphere, especially in colder regions. Section 3.2 shows our multifluid Ebysus simulation output and demonstrates close agreement with TFBI theory. Section 3.3 discusses the nonlinear stage of the simulation and investigates the resulting heating, transport, and turbulent motions. Such effects may be responsible for the discrepancy between modern models and observations of the chromosphere. The paper concludes with a summary and discussion of the results in Section 4.

2. Theory and Simulation Structure

Both the instability theory (Dimant et al. 2022; see also Appendix A) and the Ebysus (Martínez-Sykora et al. 2020) simulations in this work use multifluid models to study the chromosphere. In these models, the continuity, momentum, and energy equations govern the number density, n_s; velocity, u_s; and temperature (in energy units), T_s, for each fluid (s):

$$\frac{\partial n_s}{\partial t} + \nabla \cdot (n_s \boldsymbol{u}_s) = 0, \tag{1a}$$

$$n_s \frac{d_s \boldsymbol{u}_s}{dt} = -\frac{\nabla (n_s T_s)}{m_s} + n_s \frac{q_s}{m_s} (\boldsymbol{E} + \boldsymbol{u}_s \times \boldsymbol{B}) + \sum_j n_s \nu_{sj} (\boldsymbol{u}_j - \boldsymbol{u}_s), \tag{1b}$$

$$\frac{d_s T_s}{dt} = -\frac{2}{3} T_s \nabla \cdot \boldsymbol{u}_s + \sum_j \frac{2m_s}{m_s + m_j} \nu_{sj} \times \left[\frac{m_j}{3} (\boldsymbol{u}_j - \boldsymbol{u}_s)^2 + (T_j - T_s) \right], \tag{1c}$$

where $d_s f/dt = \partial f/\partial t + \boldsymbol{u}_s \cdot \nabla f$, and sums are taken over all fluids including electrons. The atomic mass and charge of the fluid species s are m_s and q_s, while $\boldsymbol{E}$ and $\boldsymbol{B}$ are the electric and magnetic fields, respectively. The collision frequency for momentum transfer to fluid s from fluid j is ν_{sj} for $s \neq j$, and the models assume elastic collisions. Note that these models treat each species as an ideal gas and neglect the effects of ionization and recombination, thermal conduction, and gravity.

The models also assume quasi-neutrality,

$$\sum_s n_s q_s = 0, \tag{1d}$$

and use it, instead of the electron continuity equation, to solve for n_e.

The theory closes the system via the electrostatic assumption, $\partial \boldsymbol{B}/\partial t = 0$. The mean electric field can be determined from the electron momentum equation, while perturbations of $\boldsymbol{E}$ are handled by the linear theory.

Meanwhile, the Ebysus code allows $\boldsymbol{B}$ to vary. Ebysus includes Equation (1), as well as Faraday's and Ampere's laws without displacement current:

$$\frac{\partial \boldsymbol{B}}{\partial t} = -\nabla \times \boldsymbol{E}, \tag{2a}$$

$$\mu_0 \boldsymbol{J} = \nabla \times \boldsymbol{B}, \tag{2b}$$

where $\mu_0 \approx 4\pi \times 10^{-7} N/A^2$ is the vacuum permeability constant, and $\boldsymbol{J} = \sum_s n_s q_s \boldsymbol{u}_s$ is the current density.

Ebysus determines $\boldsymbol{B}$ by updating it every time step using Faraday's law (Equation (2a)). To calculate the electric field, Ebysus solves the electron momentum equation (Equation (1b)) for $\boldsymbol{E}$, assuming negligible electron inertia: $(m_e/q_e)d_e \boldsymbol{u}_e/dt \rightarrow 0$. To determine the electron velocity, Ebysus solves for $\boldsymbol{u}_e$ using Ampere's law (Equation (2b)) and the definition of current density. Finally, at each time step, Ebysus updates the electron temperature and the other fluids' number densities, velocities, and temperatures using the corresponding equation from Equation (1). This fully closes the system of equations in the Ebysus model.

In the next sections, we discuss the instability theory, the initial conditions of the multifluid Ebysus simulation presented in this work, and the numerical methods utilized by Ebysus.

2.1. Linear Theory of the TFBI

Linear instability theory makes predictions about small perturbations in a static background. This theory considers plane waves with a real wavevector $\boldsymbol{k}$ and complex frequency ω, where all perturbations are proportional to $\exp[i(\boldsymbol{k} \cdot \boldsymbol{x} - \omega t)]$. Solutions with $\text{Im}(\omega) > 0$ are unstable with an exponential growth rate $\text{Im}(\omega)$.

This paper applies the linear theory described in Oppenheim et al. (2020) and Dimant et al. (2022). In addition to the effects present in the FB instability, this theory includes physical effects relevant in the chromosphere: thermal perturbations, arbitrary ion and electron magnetization, and accounting for arbitrarily many ion fluids.
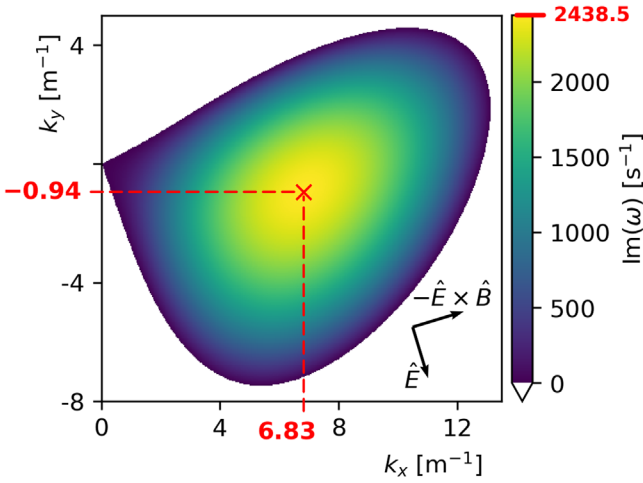
Figure 1. Predicted growth rate (Im(ω)) as a function of wavevector ($\boldsymbol{k}$) using $k_z=0$, $\boldsymbol{B} = |\boldsymbol{B}|\hat{z}$ for the parameters shown in Table 1. The black arrows in the lower right corner indicate the directions of $\boldsymbol{E}$ and $-\boldsymbol{E} \times \boldsymbol{B}$ for these conditions. The red annotations highlight the point with the maximum growth rate, indicating its value and location.

Table 1
Initial Mean Values of Simulation Parameters, Representing a Relatively Cold Region in the Chromosphere

	n (m^{-3})	u_x (m s^{-1})	u_y (m s^{-1})	T (K)	$\nu_{s,\mathrm{H}}$ (s^{-1})
e−	3.6×10^{15}	−8690	−1790	7160	1.6×10^{7}
C+	6.0×10^{14}	−1090	−4410	4830	1.4×10^{4}
H+	3.0×10^{15}	+190	−1260	4060	6.7×10^{5}
H	8.0×10^{19}	0	0	4000	$\cdots$
$\boldsymbol{B}_{\mathrm{sim}} = (10$ G$) \hat{z}$			$J_x^{(\mathrm{imposed})} = 5$ A m^{-2}		
$\Delta_x = \Delta_y = 2.5$ cm			$(N_x, N_y, N_z) = (512, 512, 1)$		

Note. The table shows the means of number density (n), x- and y-components of velocity (u_x and u_y), temperature (T), and momentum transfer collision frequency with neutrals ($\nu_{s,\mathrm{H}}$) for each fluid. The table also indicates the mean magnetic field in the simulation plane ($\boldsymbol{B}_{\mathrm{sim}}$), the imposed current ($J_x^{(\mathrm{imposed})}$) as described by Equation (3), the grid cell width in x and y (Δ_x and Δ_y), and the number of cells in the x, y, and z dimensions (N_x, N_y, and N_z).

Beyond Equation (1), we make some additional assumptions to simplify the algebra. In particular, we assume the plasma is weakly ionized and contains only one neutral fluid, n, which does not respond to any perturbations, and we neglect Coulomb collisions while assuming all other collision frequencies are constant. The weak ionization assumption is reasonable in extended regions of the lower-to-mid-chromosphere below 10,000 K, and in those regions, the Coulomb collisions are orders of magnitude smaller than collisions with neutrals (Wargnier et al. 2022, and references therein). We also assume the perturbation is electrostatic; i.e., any magnetic field response to the perturbation is negligible. Additionally, since two dimensions perpendicular to $\boldsymbol{B}$ are sufficient to reproduce the TFBI, we consider only such solutions here, enforcing $\boldsymbol{k} \cdot \boldsymbol{B} = 0$. Finally, we assume that the unperturbed values are constant in space and time. This assumption of vanishing gradients may need revisiting in the future, as gradients might provide important contributions to the instability in some parameter regimes. The equations and assumptions above lead to the dispersion relation for this model, summarized in Appendix A.

Figure 1 shows the predicted linear instability growth rate for the set of parameters in Table 1, representing a cold region from a simulated chromosphere (see Section 3.1). At each wavevector $\boldsymbol{k}$, the growth rate is the largest imaginary part of all of the solutions ω to the dispersion relation (Equation (A1a)). This prediction is calculated numerically by converting the dispersion relation to a polynomial in ω and applying a polynomial root-finding algorithm; see Appendix A for more details. The maximum growth rate of roughly Im(ω_{peak}) = 2440 s^{-1} occurs at $\boldsymbol{k}_{\mathrm{peak}} = (6.83\hat{x} - 0.94\hat{y})$ m^{-1}, where the coordinate system is defined such that the current flows toward $+\hat{x}$, the magnetic field points toward $+\hat{z}$, and $\hat{x} \times \hat{y} = \hat{z}$. This wavevector corresponds to plane waves with a wavelength of 0.91 m at an angle of roughly 8° below the $+x$-axis. This angle is 65° counterclockwise from the $\boldsymbol{E}$ direction, and the magnitude of the electric field is $|\boldsymbol{E}| = 8.9$ V m^{-1}.

The direction of $\boldsymbol{k}$ gives insight into the physical mechanisms causing the instability. The thermal effects in the

instability cause the largest growth rates for wavevectors parallel (or antiparallel) to the bisector of $-\boldsymbol{E}$ and $\boldsymbol{E} \times \boldsymbol{B}$. Meanwhile, the pure FB instability has maximum growth for wavevectors parallel (or antiparallel) to the $\boldsymbol{E} \times \boldsymbol{B}$ direction (Dimant & Oppenheim 2004; Dimant et al. 2022). The wavevector at peak growth rate $\boldsymbol{k}_{\mathrm{peak}}$ according to theory is 20° counterclockwise from the bisector of $\boldsymbol{E}$ and $-\boldsymbol{E} \times \boldsymbol{B}$ and 25° clockwise from the $-\boldsymbol{E} \times \boldsymbol{B}$ direction. This implies that for the chosen parameters, the thermal and FB effects both play an important role.

The length and timescales also help contextualize this instability. The wavelength at peak growth rate, 0.91 m, is much larger than the Debye lengths ($\lambda_{\mathrm{D},s}$ = 90, 200, and 100 μm for H+, C+, and e−, respectively) and larger than the collisional mean free paths (($\sqrt{T_s/m_s})/\nu_{s,\mathrm{H}}$= 0.02, 0.1, and 0.009 m for H+, C+, and e−, respectively). Meanwhile, the peak growth rate, Im(ω_{peak}) = 2.4 × 10^3 s^{-1}, and the wave frequency at that peak, Re(ω_{peak}) = 2.0 × 10^4 s^{-1}, correspond to timescales much smaller than those relevant to the macro-scale dynamics in the chromosphere (see, e.g., Wedemeyer et al. 2004; Pereira et al. 2013; Carlsson et al. 2019).

Note that changing the current and charged fluids' densities by the same factor while holding all else fixed does not affect the governing equations of the theory (see Equations (1) through (2), together with the assumption of negligible Coulomb collisions). If the current and charged fluids' densities decreased by a factor of 10, for example, the results of linear theory would remain exactly the same. This means that the theoretical growth rate prediction here may apply in multiple chromospheric plasma parameter regimes.

Finally, we gain further insight into this instability by considering the role of each ion species individually. Recalculating the theory using similar densities and temperatures but using H+ as the only ion species leads to smaller growth rate predictions with a peak closer to $\boldsymbol{k} = 0$. Repeating the calculation once more but this time using C+ as the only ion species leads to larger predicted growth rates that peak at larger $\boldsymbol{k}$. We conclude that both ions are important to the instability, with C+ driving the instability and H+ suppressing it.

2.2. Simulation Structure and Initial Conditions

To study a simplified case of this instability, we restrict ourselves to a 2.5D simulation, where vector quantities have three components but the simulation grid extends in two dimensions, using periodic boundary conditions including only electrons (e−), hydrogen neutrals (H), hydrogen ions (H+), and singly ionized carbon (C+). We choose parameters, summarized in Table 1, inspired by a cold region in the chromosphere where linear theory predicts the TFBI will grow. We include singly ionized carbon in particular because initial studies of the TFBI using PIC simulations and theory indicate that it is among the most important ionized species in determining the instability properties under chromospheric conditions (Oppenheim et al. 2020). Excluding other fluids simplifies the simulation and linear theory while reducing computational costs.

In Table 1, the mean values for the ion densities and magnetic field, and neutral density, velocity, and temperature, were chosen to represent a relatively cold region from a 2.5D radiative single-fluid MHD simulation of the chromosphere (see Section 3.1). The mean electron density satisfies quasi-neutrality (Equation (1d)). The other initial mean velocities and temperatures are selected numerically such that the mean accelerations ($\partial \boldsymbol{u}_s / \partial t$) and temperature variations ($\partial T_s / \partial t$) of all other fluids are as close to zero as possible. These velocity and temperature selections bring the simulation conditions closer to the physics described by the theory, which assumes constant mean values. The electric field is determined by the electron momentum equation assuming negligible electron inertia; initially, $\boldsymbol{E}(t=0) = (2.58\hat{x}-8.53\hat{y}) \, \mathrm{V \, m^{-1}}$, although later, $\boldsymbol{E}$ changes as shown in Appendix C.

The momentum transfer collision frequencies are calculated self-consistently following the formalism of Wargnier et al. (2022, and references therein). In particular, the (H+, H) collisions take into account the charge exchange resonance and are treated as non-Maxwellian. The (C+, H) collisions are treated assuming Maxwell molecules. The (e−, H) collision frequency is calculated by performing the collision integral over experimentally determined differential cross sections. Coulomb collision frequencies would be orders of magnitude smaller than the other collision frequencies due to the small ionization fraction; however, Coulomb collisions were instead turned off to simplify comparison between this simulation and the linear theory.

The TFBI must be driven by some energy source in order to grow. Given the chromospheric conditions selected in Table 1, for a 2.5D multifluid simulation, a sufficient source of energy can come from a current flowing across the box. Such a current can be caused by magnetic field lines bending out of the plane,

$$\boldsymbol{B} = \boldsymbol{B}_{\mathrm{sim}} - z\mu_0 J_x^{(\mathrm{imposed})}\hat{y}, \qquad (3a)$$

where the simulation box is in the xy-plane, $z = 0$; $\boldsymbol{B}_{\mathrm{sim}} = \boldsymbol{B}(z=0)$ is the magnetic field in the simulation; and $J_x^{(\mathrm{imposed})}$ is some arbitrary value that determines the magnetic field line curvature. Bending the field lines affects the simulation only through spatial derivatives in $\boldsymbol{B}$, which only appear in the Ebysus model through Ampere's law (Equation (2b)). Plugging Equation (3a) into Ampere's law

yields

$$\mu_0\boldsymbol{J} = \nabla \times \boldsymbol{B}_{\mathrm{sim}} + \mu_0 J_x^{(\mathrm{imposed})}\hat{x}. \qquad (3b)$$

Currents and magnetic field curvature in the chromosphere arise due to many different physical processes, including bulk neutral flows dragging electrons and ions across magnetic field lines, Poynting from flux emergence, colliding flows, shocks, jets, waves, and reconnection (see, e.g., Abbett 2007). To focus on resolving the TFBI, rather than any of these processes, we impose a current in the simulation, as modeled by Equation (3). One might conceptualize this current as the simulation box being placed perpendicular to the curving magnetic field formed from a shock, reconnection, or some other process.

In our simulation, $\boldsymbol{B}_{\mathrm{sim}}$ is constant except for a small spatial perturbation, with perturbation strength (the ratio between standard deviation and mean) peaking at 2.2×10^{-3} and always remaining less than 1.1% of the electron density perturbation strength. Because the mean of $\boldsymbol{B}_{\mathrm{sim}}$ is constant in time, the imposed current term provides the mean value for the current density throughout the simulation.

We chose an imposed current density of $5 \, \mathrm{A \, m^{-2}}$ for the multifluid simulation to reduce computational costs. This current is roughly 10 times larger than any currents found in the macro-scale simulated chromosphere discussed in Section 3.1. However, changing the current does not affect the linear theory of the TFBI if all of the charged fluids' densities also change by the same factor, as discussed in Section 2.1. Ion and electron densities vary across many orders of magnitude in the simulated chromosphere, in some regions reaching at least 10 times smaller than those in Table 1. Thus, while the simulation current density may be larger than typical in the chromosphere, the linear regime of the multifluid TFBI simulation here should still accurately model some regions of the chromosphere, particularly those with current and charged fluids' densities decreased by the same factor with all else held fixed.

While the imposed current is sufficient to drive the TFBI for our simulation, the instability does not directly require it. Rather, the instability requires sufficiently large sustained drifts relative to neutrals, perpendicular to the magnetic field. However, we also note that removing the imposed current from our simulation causes the necessary velocity differences to vanish significantly faster than the instability growth rate. This behavior is consistent with Dimant et al. (2016), which detailed the criterion for generating currents from neutral flows in a weakly ionized collisional plasma.

2.3. Numerical Scheme

Ebysus (Martínez-Sykora et al. 2020) is a multifluid radiative electromagnetic simulator designed to model the Sun's chromosphere. Here we describe only the parts of the code used in our study of the TFBI. For example, the Ebysus simulations here only utilize explicit methods, so we do not discuss the operator splitting option for semi-implicit time evolution. Some of the architecture and methodology in Ebysus are inherited from Bifrost (Gudiksen et al. 2011).

Ebysus utilizes a third-order predictor–corrector Hyman explicit time-step method (Hyman 1979) to calculate derivatives with respect to time. The numerical domain is defined in a staggered mesh with scalars at grid cell centers and vector components centered on cell edges or faces. As necessary,

interpolation is performed using a fifth-order scheme. Meanwhile, spatial derivatives are computed using a sixth-order scheme. The details of the staggered mesh, interpolation, and derivative calculations match those of Bifrost.

Ebysus also includes artificial hyperdiffusion terms for stability that primarily diffuse sharp fluctuations at small scales (five grid cells or less). These terms are similar to those in Bifrost but have been adapted to the multifluid model. Their exact forms are detailed in Appendix B.

3. Results

Section 3.1 discusses the predicted growth rate for the TFBI throughout the chromosphere. This result comes from applying the linear theory to a single-fluid macro-scale simulation and predicts that the instability occurs throughout many of the relatively cold regions in the chromosphere. Section 3.2 presents the main multifluid simulation in this work and analyzes the simulation growth rates to confirm they match closely with theory. Section 3.3 demonstrates that this instability leads to increased temperatures and fluctuations in speed, as well as varied mean velocities, for all fluids in the simulation. Taken together, these results indicate that the effects of the TFBI may significantly affect heating, transport, and turbulent motions throughout the colder regions in the chromosphere.

3.1. Predicting Regions of Instability in the Chromosphere

To predict where the TFBI occurs throughout the chromosphere, we combine the linear instability theory with output from a single-fluid macro-scale simulation run using the rMHD code, Bifrost (Gudiksen et al. 2011). This single-fluid simulation treats hydrogen and helium ionization and recombination in nonequilibrium (Leenaarts et al. 2007; Golding et al. 2016) and incorporates some of the effects of interactions between ions and neutrals by including ambipolar diffusion (Nóbrega-Siverio et al. 2020). Our prediction improves upon the related prediction in Oppenheim et al. (2020) by solving the full multifluid linear theory including thermal perturbations and utilizing output from a Bifrost simulation that included nonequilibrium ionization modeling.

For this work, we convert the single-fluid Bifrost simulation output into a set of multifluid parameters including only H, H +, C+, and electrons. The magnetic field, along with the H and H+ density, comes directly from the Bifrost simulation output, as the densities were tracked via the nonequilibrium ionization modeling. The temperatures of all fluids are set equal to the simulated single-fluid temperature for simplicity. The neutral velocity is set to zero, while the velocities of charged fluids come from the ambipolar velocity (Pederson drift), as detailed in Martínez-Sykora et al. (2012). Finally, the C+ density is set to the appropriate fraction of the single-fluid density, assuming photospheric abundances to find the density of carbon (Asplund et al. 2009) and statistical equilibrium to determine its ionization fraction.

Figure 2 shows the resulting growth rate prediction for the TFBI throughout the simulated chromosphere. At each point in space, the growth rate is determined by taking the largest imaginary part of all of the solutions for ω across a variety of k. We tested all values of k with magnitude 0.1, 0.3, 1, 3, 10, 30, 100, or 300 [m^{-1}] and each of 18 directions separated by 1° increments in the plane perpendicular to the local magnetic field. Points with a negative growth rate are shown in gray. Note in particular that the predicted instability growth is correlated with the colder temperatures in the chromosphere.

At every location with predicted growth, the single-fluid MHD model may be inaccurate, as it fails to incorporate the effects of the TFBI. Combined with the prediction of heating due to the TFBI (see Figure 6 in the next section), this supports the possibility of the TFBI being responsible for the missing heating in chromospheric models.

White regions in Figure 2 indicate where the assumptions of the TFBI theory break down, and the growth rate was not calculated. In the upper chromosphere and above, white regions indicate areas where the plasma does not satisfy the weakly ionized assumption, defined here as $n_{\mathrm{ion}}/n_{\mathrm{neutral}} < 0.01$. In the lower chromosphere and below, white regions indicate areas where the electrons are not strongly magnetized, having $|q_e||\boldsymbol{B}|/(m_e \nu_{e,\mathrm{H}}) < 2$. In regions of weakly magnetized or demagnetized electrons, we discovered that the TFBI theory sometimes predicts instability growth (not shown on the plot); however, it is only for large wavelengths ($|\boldsymbol{k}| \lesssim 0.01\,\mathrm{m}^{-1}$) and long timescales ($\mathrm{Im}(\omega) \lesssim 0.001\,\mathrm{s}^{-1}$). We mask these results because the lower solar atmosphere may be dynamic on such timescales (see, e.g., Wedemeyer et al. 2004; Pereira et al. 2013; Carlsson et al. 2019), which invalidates the assumption of constant background as required by the linear theory. Furthermore, any physical mechanisms responsible for instability involving demagnetized electrons may be different than those responsible for the TFBI.

While Figure 2 suggests that the TFBI occurs ubiquitously throughout the colder regions in the simulated chromosphere, there are a few causes for concern about whether the predicted growth rates are similar to those in the actual chromosphere. First, the underlying Bifrost simulation does not correctly represent the physics of TFBI, and incorporating such effects may produce different results. In particular, large electric fields develop in Bifrost that indicate hypersonic drifts. These probably would be mitigated by the TFBI. The instability would also cause heating and changes in velocity. Second, the assumptions that we applied to convert the single-fluid Bifrost simulation output into a set of multifluid values for the TFBI theory could make these predictions inaccurate. Third, gradients (e.g., in number density or temperature) are not included in the theory presented here, which assumes a constant background, but such gradients may affect the wave properties and growth rates.

To investigate a few possible issues with the assumptions of the prediction in Figure 2, we consider in particular the temperatures and the mixture of fluids used for the calculation. We predicted TFBI growth predominantly in Bifrost regions with temperatures significantly less than the minimum suggested by observations (da Silva Santos et al. 2020). To test the extent of our prediction's dependence on these unphysically low temperatures, we repeat the linear theory calculation but artificially set temperatures less than 4000 K to this minimum value. This change has minimal impact, yielding a positive growth rate prediction in over 95% of the same regions and altering the average positive growth rate by only a factor of 2. We argue that single-fluid rMHD codes exhibit unphysically low temperatures as a result of their oversimplifications of chromospheric physics, such as the exclusion of TFBI effects.
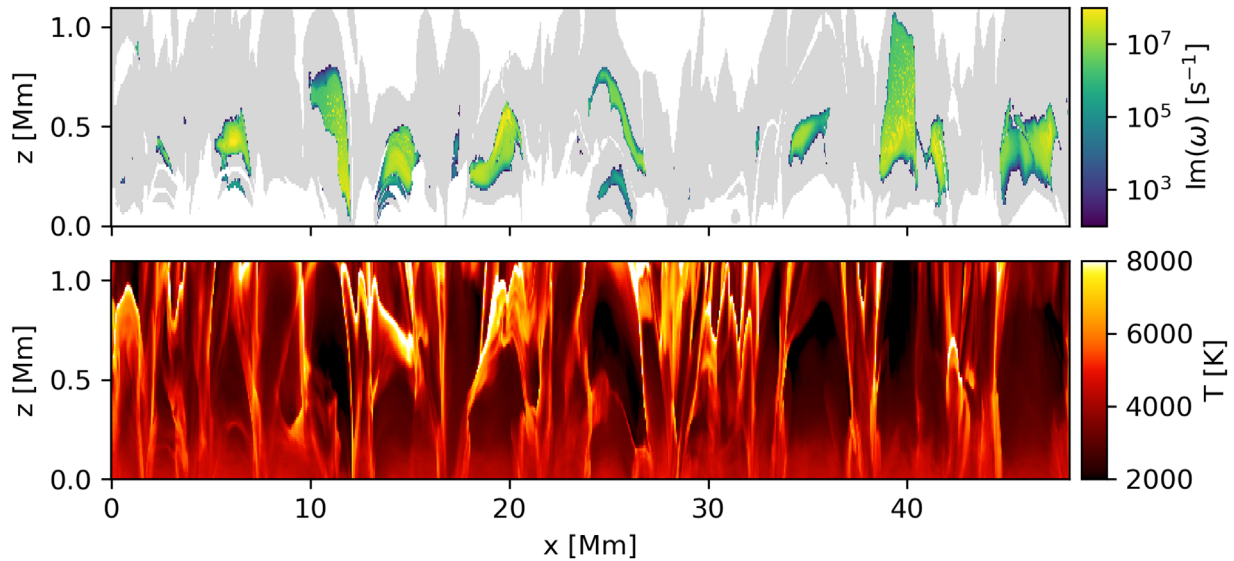
Figure 2. (Top) Growth rate of the multifluid TFBI throughout the chromosphere from a Bifrost simulation snapshot. The gray regions represent tested points with negative growth rates. The white regions show untested points where the assumptions of the TFBI theory are not satisfied. Note that x spans 50 Mm, while the z direction ranges from zero at the photosphere up to 1.1 Mm. (Bottom) Temperatures from the same Bifrost simulation snapshot. Many of the colder regions overlap with locations of predicted growth of the TFBI.
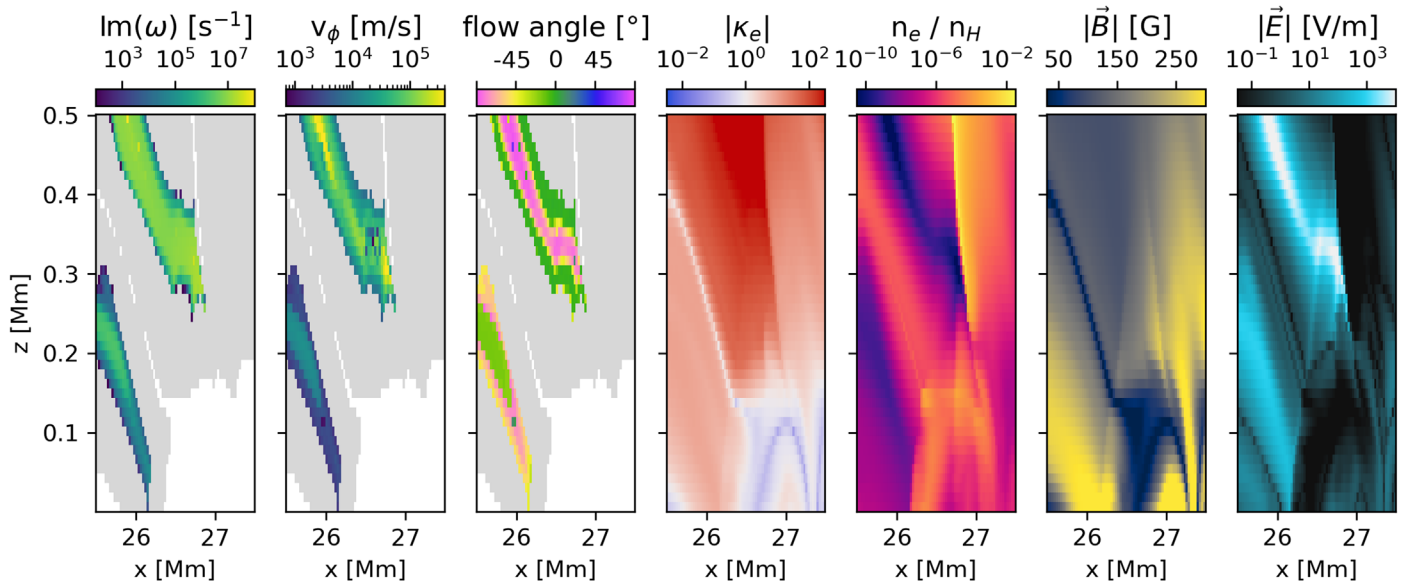
Figure 3. Various parameters plotted in the region 25.5 Mm $< x <$ 27.5 Mm, 0 Mm $< z <$ 0.5 Mm using the same Bifrost snapshot as in Figure 2. From left to right, these panels show the predicted growth rates when testing more values of $\boldsymbol{k}$ than used in Figure 2; the phase speed, $v_\phi = \mathrm{Re}(\omega)/|\boldsymbol{k}|$; the flow angle, i.e., the angle from $\boldsymbol{E} \times \boldsymbol{B}$ to $\boldsymbol{k}$ or $-\boldsymbol{k}$, whichever is closer; the electron magnetization, $|\kappa_e| = |q_e||\boldsymbol{B}|/(m_e \nu_{e,\mathrm{H}})$; the ionization fraction, n_e/n_H; the magnetic field magnitude, $|\boldsymbol{B}|$; and the electric field magnitude, $|\boldsymbol{E}|$. In the first three panels, gray indicates negative growth rate predictions, while white corresponds with untested points where the TFBI assumptions break down.

To make the prediction in Figure 2, we assumed a mixture of only electrons, neutral H, H+, and C+ fluids, which is an oversimplification of the chromospheric composition. This assumption simplifies computations and allows comparison with the multifluid TFBI simulations, which become significantly more expensive if run using all major ions in the chromosphere. To test that we still capture the dominant physics with this reduced set of ions, we calculate the TFBI growth rates for a system that adds Fe+ to the mixture above. This somewhat alters the results but still predicts TFBI growth throughout the chromosphere. We argue that assuming an even more realistic mixture including more fluids may further alter the details of the results but would leave the key point

unchanged; based on this Bifrost simulation, the TFBI could occur throughout the chromosphere.

Due to the limitations of this analysis and the Bifrost model, we further explore these predictions in Figure 3. This figure shows various parameters in one particular area where there are two distinct regions of predicted instability growth. First, we check that the previous prediction was not missing any significant regions of instability by sweeping across more possible values of $\boldsymbol{k}$. The first panel of Figure 3 shows the predicted growth rates after checking values of $\boldsymbol{k}$ with each of the 24 mag between 0.1 and 681 [m^{-1}] (inclusive) with even logarithmic spacing and each of the 60 directions separated by 3° increments in the plane perpendicular to the local magnetic

field. This more accurate search predicts that the instability will occur in the same regions as in Figure 2, though with slightly larger growth rates.

The second and third panels of Figure 3 further characterize the predicted wave properties in this region. The second panel shows the phase speed, $v_\phi = \mathrm{Re}(\omega)/|\boldsymbol{k}|$. The third panel shows the flow angle, the angle from $\boldsymbol{E} \times \boldsymbol{B}$ to $\boldsymbol{k}$ or $-\boldsymbol{k}$, whichever is closer. This angle gives insight into which effects contribute to the instability. In the single-species ion case with strongly magnetized electrons and weakly magnetized ions, pure FB waves have a flow angle near $0°$, while waves dominated by thermal effects have a flow angle close to $-45°$, the bisector of $-\boldsymbol{E}$ and $\boldsymbol{E} \times \boldsymbol{B}$ (Dimant & Oppenheim 2004; Dimant et al. 2022). For example, around the edges of the lower left region of predicted instability (within $x < 26.3$, $z < 0.3$ Mm), the flow angle suggests that thermal effects dominate. Meanwhile, in the middle (furthest from any edges) parts of this region, the flow angle suggests significant contributions from both thermal and FB effects, requiring the TFBI theory for an accurate description.

The remaining panels in Figure 3 provide some other physical parameters for reference. The fourth panel provides the electron magnetization, $|\kappa_e| = |q_e||\boldsymbol{B}|/(m_e \nu_{e,H})$, which is larger than 2.0 for all nonwhite points in the first three panels. The fifth panel shows the ionization fraction, n_e/n_H, which is smaller than 0.01 for all nonwhite points in the first three panels. The sixth panel plots the magnitude of the magnetic field, $|\boldsymbol{B}|$, with values of up to a few hundred gauss consistent with observations (see, e.g., Trujillo Bueno et al. 2006; Ishikawa et al. 2021). While the magnetic field in this area is greater than 10 G everywhere with predicted TFBI growth, the larger area from Figure 2 contains some regions of predicted instability that coincide with magnetic fields of 10 G or less. Despite the relatively small magnetic field, we chose parameters for our TFBI simulation (see Table 1) inspired by these regions because they seemed most likely to produce the instability using the least amount of computational time. The final panel shows the magnitude of the electric field, $|\boldsymbol{E}|$, which reaches more than 1000 V m^{-1} in some regions; such large electric fields could be mitigated by the presence of the TFBI, which is not incorporated into the Bifrost simulation.

3.2. Simulation of the Instability

We use Ebysus to run a multifluid simulation of a relatively cold region in the chromosphere with magnetic field lines bent out of the plane using the parameters in Table 1. This simulation shows a clear wave pattern similar to that found in kinetic simulations (Oppenheim et al. 2020). The growth rate agrees with linear theory during the linear regime, indicating an accurate reproduction of the TFBI. This success demonstrates that multifluid simulators are capable of producing the TFBI.

Figure 4 and the corresponding animation show the electron number density throughout the simulation. We initialize the number density at $t = 0$ (top left panel) with a random perturbation having a standard deviation approximately 4.6 orders of magnitude smaller than the background density, smoothed by a Gaussian kernel to mitigate numerical artifacts at the grid scale. A clear wave pattern develops by $t = 1.0$ ms (top middle panel), and the perturbation grows according to linear theory. By $t = 3.0$ ms (top right panel), the perturbation has grown by roughly 2 orders of magnitude. At around $t \approx 5.2$ ms (bottom left panel), nonlinear effects start to develop

as the perturbation becomes comparable in magnitude to the mean density, 3.6×10^{15} m^{-3}.

Around $t \approx 5.3$ ms, the rms perturbation reaches its maximum of roughly 27% of the background value, though it eventually settles down to roughly 17% by the end of the simulation. The bottom middle panel of Figure 4 shows that by $t = 5.6$ ms, secondary waves have developed and spread throughout the simulation box. From this time onward, the linear-stage TFBI is no longer the dominant effect in the simulation. Finally, the bottom right panel shows the density when the simulation ends at $t = 7.9$ ms. By the end of the simulation, the perturbations reach a quasi-steady state where the amplitude and scale size of features settle to roughly constant values.

To confirm that this simulation really does reproduce the TFBI, Figure 5 compares growth rates from the simulation to linear theory. To determine the growth rates, we compute a Fourier transform in space at each snapshot in time, $\mathcal{F}_t(\boldsymbol{k})$, of the electron number density perturbation from $t = 0.6$ to 1.9 ms. According to linear theory, the magnitude at each $\boldsymbol{k}$ should scale as $\exp[\mathrm{Im}(\omega)t]$. Thus, for each $\boldsymbol{k}$, the slope of the best-fit line through the natural log of the magnitude of the Fourier transforms provides the simulation growth rate, $\gamma = \mathrm{Im}(\omega)$, as follows:

$$\gamma\, t + \mathrm{offset} = \ln|\mathcal{F}_t(\boldsymbol{k})|. \tag{4}$$

The left panel of Figure 5 plots the results of this fitting process. The right panel of the figure compares the simulation and theory directly by overlaying contours of γ as determined here for the simulation and in Section 2.1 for the theory.

Figure 5 shows remarkably close agreement between simulation and linear theory. Qualitatively, the simulation and linear theory contours are almost aligned and have similar but slightly different shapes. The difference in shapes is not too concerning, as the morphology varies with the parameters in linear theory (Dimant et al. 2022 contains some examples). Meanwhile, comparing quantitatively at the peak growth rates, the simulation growth rate $\omega_{\mathrm{peak}}^{(\mathrm{sim})}$ is 6.6% less than ω_{peak} in the theory. The magnitude of the wavevector at the simulation peak $|\boldsymbol{k}_{\mathrm{peak}}^{(\mathrm{sim})}|$ is 9.6% smaller than in the theory, and its direction $\boldsymbol{k}_{\mathrm{peak}}^{(\mathrm{sim})}$ differs from the theory peak by $10°.8$. From this close agreement, we conclude that this simulation does indeed reproduce the TFBI described by linear theory.

A small discrepancy still remains between the simulated and predicted growth rate versus wavevector distributions. One possible source of error is the changing background quantities. In particular, the linear theory neglects any zeroth-order acceleration ($d_s \boldsymbol{u}_s/dt$) and temperature variations ($d_s T_s/dt$). Meanwhile, some background acceleration and heating in the simulation is an unavoidable consequence of the imposed current (see Equation (3)), although the amount depends on the simulation parameters.

To check whether the zeroth-order effects of the imposed current are the main source of the discrepancy, we repeated the simulation but used imposed current and ion number densities 10 times larger (not shown here). This change of parameters has almost no effect on the theoretical prediction while increasing the zeroth-order acceleration and heating of all electrons and ions by a factor of 10. The discrepancy between simulation and theory also increases significantly. Quantitatively, at the peak for this test simulation, the growth rate is 11.6% less than in the theory (compared with 6.6% from the

$$\delta n_e \ [\ 1 / m^3 \ ]$$
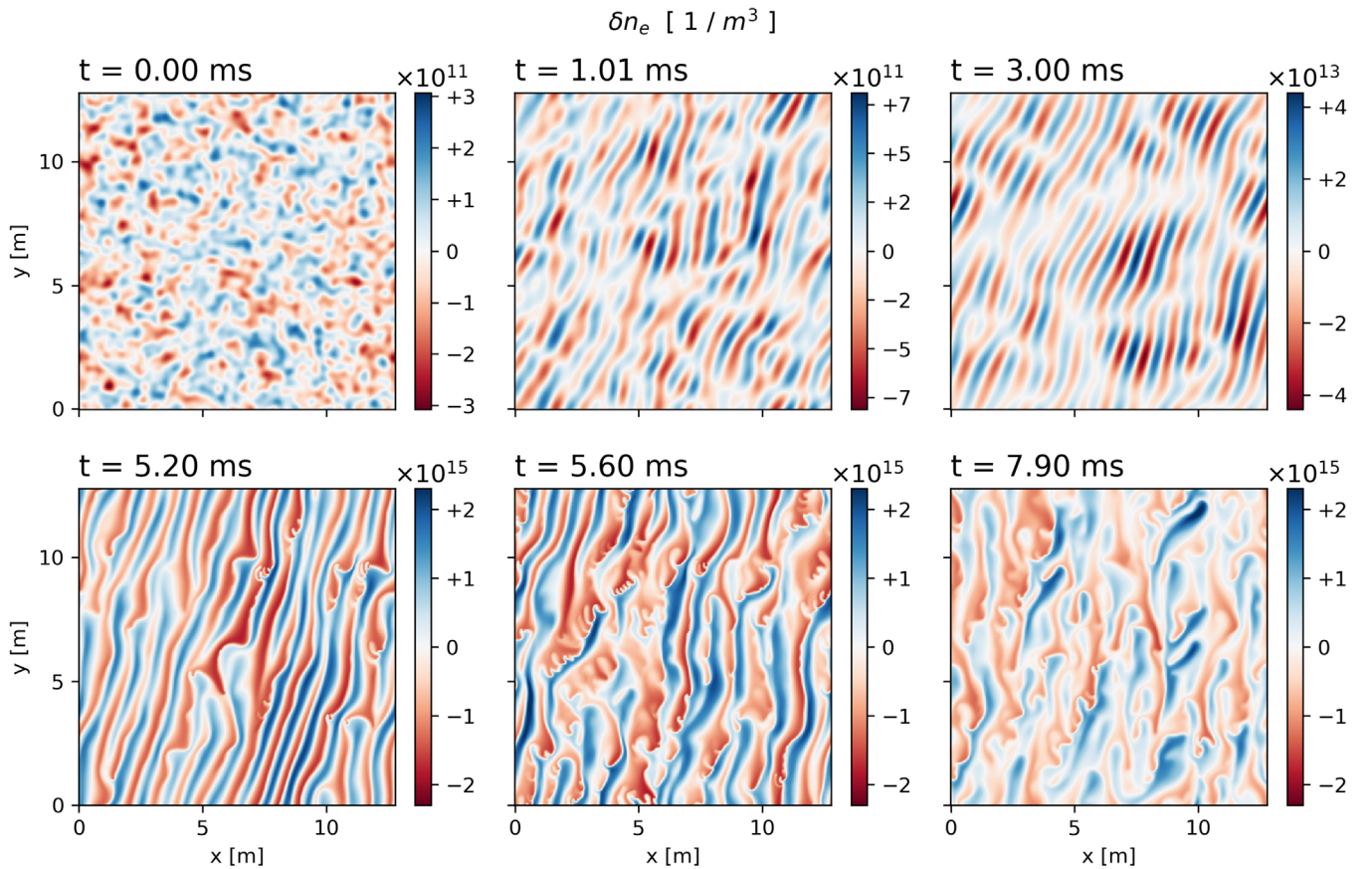
Figure 4. Perturbation of electron number density at selected snapshots throughout the simulation. The associated movie available online (duration: 18 s) shows the evolution throughout the entire simulation. The simulation runs from $t = 0.0$ to 7.90 ms. Note that the color scale varies between panels in this figure and in time in the animation. Panels (or frames in the animation) show snapshots of the simulation at different stages, including the initial conditions, linear growth phase, and nonlinear regime.

(An animation of this figure is available.)

main simulation), $|\mathbf{k}|$ is 7.4% smaller than in the theory (compared with 9.6%), and the direction of $\mathbf{k}$ differs from the theory peak by 14°.7 (compared with 10°.8). We conclude that the zeroth-order acceleration and heating terms are the most likely main source of error in the original simulation.

Other possible sources of error include electromagnetic effects, which are included in the simulation but not the theory, and any artifacts of the numerical method used for the simulation. The small magnetic field fluctuations, with a relative size less than 1% compared to the relative size of the density fluctuations, suggest that the electromagnetic assumption does not introduce a sizable error. Meanwhile, we found the numerical diffusion effects to be small, especially during the linear growth stages of the simulation, implying at most minor error contributions from numerical artifacts.

The linear stage of the main TFBI simulation confirms that the instability occurs for the chromospheric parameters in Table 1, as well as for any similar plasma with the same ratios of current and charged fluids' densities. In particular, the simulation also reproduces the linear stage of the TFBI for such plasma because the linear theory is unaffected by changing current and charged fluids' densities by the same factor. Additionally, the trend from the test simulation (10 times larger $\mathbf{J}$, n_e, n_{H+}, and n_{C+} than in Table 1) to the main simulation (values directly from Table 1) suggests that similar simulations with even smaller current and charged fluids' densities would

have even better agreement between the linear regime of the simulation and the linear theory.

In the next section, we analyze the effects of turbulence throughout this simulation. While we are confident that this simulation accurately represents the linear regime for any similar plasma with the same ratios of current and charged fluids' densities, it is not yet clear how the nonlinear behavior would be altered by using different parameters.

### 3.3. Effects of Turbulence: Heating, Transport, and Turbulent Motion

While the linear theory fully breaks down at around $t = 5.2$ ms in our simulation of the TFBI, turbulence affects the temperatures and velocities of fluids as soon as $t = 4.0$ ms, when the rms electron density perturbation reaches approximately 3% of the mean electron density. These nonlinear effects do not arise physically in macro-scale models that fail to resolve the small scales (a few meters and a few milliseconds) and to include the multifluid physics relevant to the TFBI. Therefore, the effects of the TFBI might cause disagreements when comparing such models to solar observations. In this section, we use our simulation to investigate the turbulence-driven heating, transport, and turbulent motions due to the TFBI.

Figure 6 illustrates the turbulence-driven heating in the simulation. The plots show the evolution of fluid temperatures
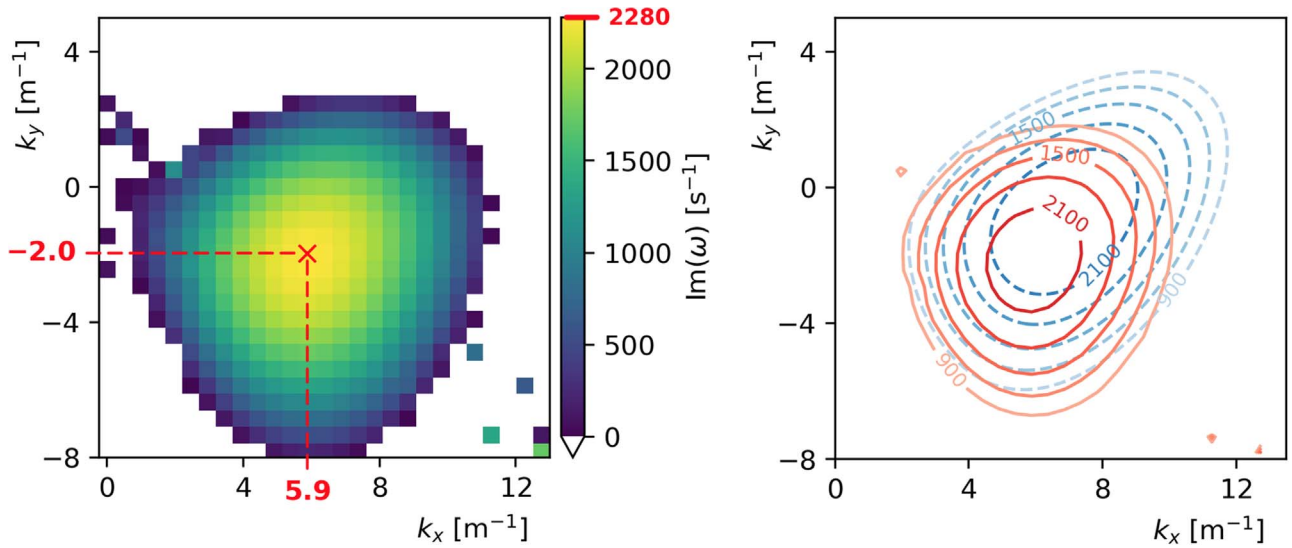
Figure 5. (Left) Growth rate as a function of wavevector, calculated using simulation outputs during the linear growth stage. (Right) Contours of the growth rate vs. $\boldsymbol{k}$ map from the simulation (red solid lines) and the theoretical prediction from Figure 1 (blue dashed lines), labeled with values in units of s^{-1}. The close agreement supports the claim that this simulation reproduces the TFBI. The remaining discrepancy between theory and simulation is addressed further in the main text.
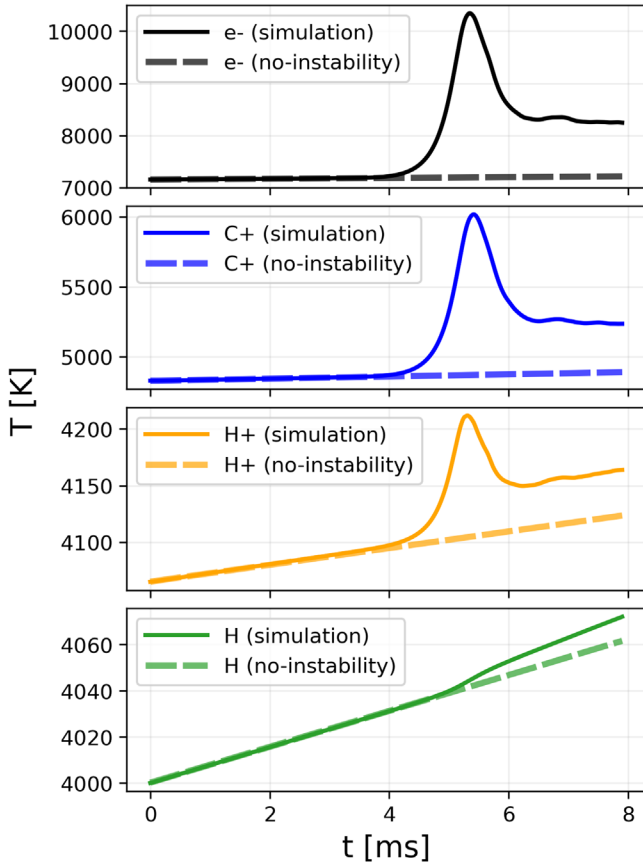
Figure 6. Temperature evolution of each fluid throughout the simulation of the TFBI. Solid lines show mean temperatures throughout the simulation. Dashed lines show temperature predictions using the same physical parameters but without accounting for the instability. Linear theory alone predicts no change in mean temperatures due to the instability; around $t = 4.0$ ms, nonlinear effects start to become important and cause heating.

throughout the simulation, as well as the temperature evolution predictions for a no-instability model with the same physical parameters as in the simulation (shown in Table 1) but that lacks the spatial resolution to reproduce the TFBI. These no-instability temperature predictions are constructed by plugging mean values of quantities into the energy Equation (1c) to calculate $\partial T_s / \partial t$ from $t = 0$ to 0.5 ms—when the instability effects become relevant—then extrapolating linearly until the end of the simulation. The no-instability model shows constant nonzero heating due to the imposed current (see Equation (3)).

There is significant heating due to the TFBI. In the simulation, the electron temperature overshoots up to 3000 K more than its original value of 7000 K before settling down to about 8300 K, 1300 K above the original temperature. The ion temperatures look qualitatively similar; C+ peaks at an increase of 1200 K before settling to 400 K above the no-instability model temperature, while H+ peaks at an increase of 100 K and settles to an increase of 30 K. The neutral temperature does not overshoot but ends up approximately 10 K larger by the end of the simulation due to thermal energy transfer from collisions with the charged fluids heated by the TFBI. This heating may contribute toward heating the actual chromosphere and help explain why macro-scale models such as Bifrost predict temperatures thousands of kelvins smaller than those implied by observations.

The heating comes from collisional effects. Collisions convert the kinetic energy into thermal energy and allow thermal energy transfer between fluids. The dissipation of velocity drifts heats the ions and electrons, though a majority of that thermal energy transfers into the neutrals. Still, the neutral temperature changes less than the other fluids' temperatures during the simulation because the neutrals are multiple orders of magnitude denser. By the end of the simulation, the charged fluids' temperatures reach a constant difference with their no-instability counterparts, but the neutral temperature keeps increasing. If the simulation were to run longer, we predict this quasi-steady state would continue, as all of the turbulence-driven heating of charged fluids transfers energy into the neutrals. As long as the TFBI turbulence continues, electron and ion temperatures will remain elevated. Eventually, conditions would change significantly enough to dampen the TFBI, possibly after heating the neutrals by hundreds or thousands of kelvins.
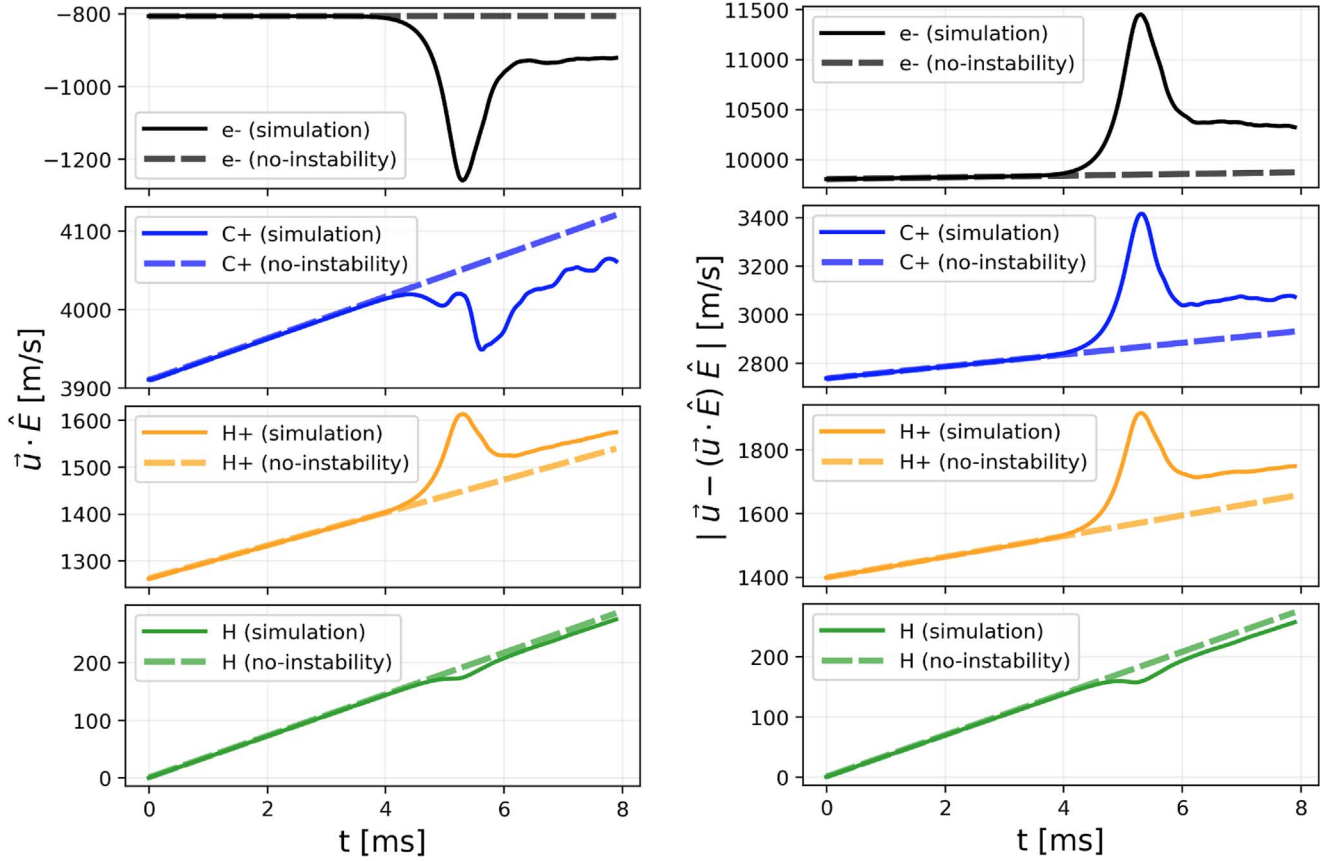
Figure 7. Velocity evolution throughout the TFBI simulation for each fluid (electrons, C+, H+, and H, from top to bottom). Solid lines show mean velocities throughout the simulation. Dashed lines show velocity predictions using the same physical parameters but not accounting for any instability. The left panels show the velocity component in the electric field direction, $\boldsymbol{u} \cdot \hat{E}$, while the right panels show the component perpendicular to the electric field, $|\boldsymbol{u} - (\boldsymbol{u} \cdot \hat{E})\hat{E}|$, where $\hat{E} = \boldsymbol{E}/|\boldsymbol{E}|$. Linear theory alone predicts no change in mean velocities due to the instability; around $t = 4.0$ ms, nonlinear effects start to become important and cause acceleration.

Figure 7 illustrates the turbulence-driven transport in the simulation. The plots show the evolution of the fluids' velocities throughout the simulation, broken up into components parallel and perpendicular to the mean electric field. Similarly to Figure 6, these plots also compare to a no-instability model, constructed here by plugging mean values into the momentum Equation (1b) to calculate the accelerations until $t = 0.5$ ms, then extrapolating linearly after that time. The no-instability model has a nonzero slope due to the imposed current (see Equation (3)).

There is moderate transport due to the TFBI in this simulation. For each velocity component of each fluid, the nonlinear effects are not apparent until roughly $t = 4.0$ ms, at which point the behavior changes, leading to an overshoot and then settling toward some particular deviation from the no-instability model. Parallel to $\boldsymbol{E}$, the electrons end up with a velocity of roughly -920 m s^{-1}, 120 m s^{-1} less than the no-instability model predicts. The ion and neutral velocities in this direction all differ from the no-instability model by less than 5%. Perpendicular to $\boldsymbol{E}$, the electrons end up with a simulation mean velocity that is roughly 450 m s^{-1} (5%) larger due to the instability. The ion velocities in this direction increase by roughly 5% due to the instability, while the neutral velocity decreases by roughly 5%.

Altering the mean velocities affects the electric field strength and direction. Electrons traveling parallel to $\boldsymbol{E}$ work to short out the field, while those traveling perpendicular to $\boldsymbol{E}$ increase

the field. For our simulation, the impact of increased perpendicular transport is stronger than the change in transport parallel to $\boldsymbol{E}$, leading to an increased electric field magnitude, as shown in Appendix C. To incorporate these effects into a macro-scale model, more work is required to determine the behavior of instability-driven transport and electric field changes across a range of parameters. Eventually, these effects could be modeled by parametrically adjusting electron and ion collision frequencies with neutrals, altering the effective cross-field conductivities.

Figure 8 shows the turbulent motions of each fluid throughout the main multifluid simulation. These motions are computed by taking the standard deviation of the speed (i.e., magnitude of velocity) for each fluid at each simulation snapshot. Similarly to the turbulence-driven heating, the turbulent motion speeds of all of the charged fluids overshoot, then settle down to some value above a baseline. The relevant baseline in this case is zero; a model lacking the resolution to consider fluctuations would see zero deviation from the mean caused by effects at this scale.

There are notable turbulent motions due to the TFBI. The standard deviation of the electron speed overshoots to 5200 m s^{-1} before settling to roughly 2500 m s^{-1}. For C+, the peak is around 1150 m s^{-1} before settling to roughly 750 m s^{-1}. For H+, the peak is at 900 m s^{-1}, and the turbulent motion speed decreases to 400 m s^{-1} by the end of the simulation. The neutral speed does not overshoot but ends up at
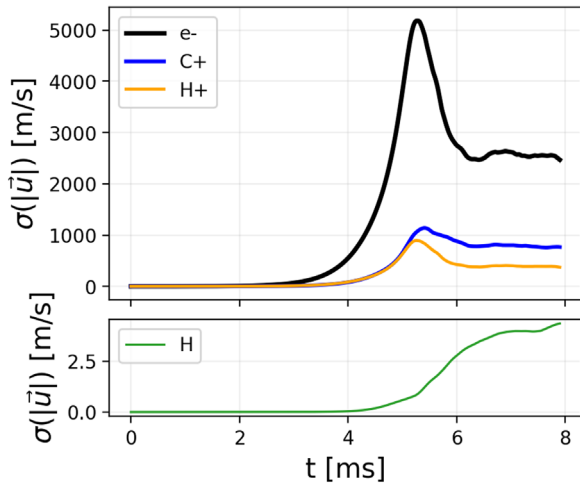
Figure 8. Turbulent motions of each fluid throughout the simulation of the TFBI. The y-axis shows the standard deviation of the fluid speed and is split into top and bottom plots with different scaling so that the changes for neutral hydrogen are visible.

approximately $4\,\mathrm{m\,s^{-1}}$ due to collisions with the other fluids in the simulation. Turbulent motions due to small-scale effects such as the TFBI could contribute to broadening chromospheric spectral lines in observations.

4. Conclusions

Combining the linear instability theory of a multifluid model and the output of a single-fluid simulation, this work predicts that the TFBI occurs throughout many of the colder regions in the chromosphere. This prediction improves upon the related prediction in Oppenheim et al. (2020) by solving the full multifluid linear theory, including thermal perturbations, and utilizing output from a Bifrost simulation that included nonequilibrium ionization modeling. Our estimates reveal that the single-fluid rMHD model has extended regions that may be inaccurate, since the model does not incorporate the effects of the TFBI.

Focusing on the parameters found in one of these colder regions in the chromosphere, we produce the first multifluid simulation of the TFBI. We validate this by showing close agreement between the simulation and linear theory. For computational reasons, we used a current density that is too large by roughly an order of magnitude compared to those in the single-fluid simulated chromosphere. This adjustment does not affect the linear theory but likely contributes to the small error between simulation and theory during the linear regime. The ability to produce this instability with a multifluid code enables further study of the instability across chromospheric parameter ranges that are computationally challenging for kinetic models.

Our multifluid simulation exhibits turbulence-driven heating, transport, and enhanced turbulent motions of all fluids in the simulation. The significant heating supports the possibility that the TFBI may contribute toward chromospheric heating. The transport will modify cross-field conductivities and electric fields. The turbulent motions, having speeds consistent with the microturbulence inferred from inversions of observations (da Silva Santos et al. 2020), may help to explain why observations show broader Mg II h and k lines than synthetic spectra from highly successful numerical models of the lower solar atmosphere (Hansteen et al. 2023; Martínez-Sykora et al.

2023). However, nonlinear effects may differ for different sets of parameters throughout the chromosphere. Additionally, these turbulent behaviors could change significantly for a 3D simulation, where the possibility for a turbulent electric field component parallel to $\boldsymbol{B}$ could greatly increase electron heating. Quantitatively determining the impacts of the TFBI throughout the chromosphere may require a suite of small-scale multifluid simulations, some in 3D, spanning a wide range of parameters.

The nonlinear effects caused by the TFBI occur on scales of meters and milliseconds—far smaller than what has been resolved by macro-scale simulations of the Sun's atmosphere—yet they may play an important role in explaining observations of chromospheric heating and line broadening due to turbulent motion. These effects motivate further study of the TFBI and its impact throughout the chromosphere.

Appendix A
Linear Multifluid Instability Theory

Starting with fluid Equation (1), one may derive a theoretical prediction for the properties of linear waves. This is done by linearizing the equations and assuming that the original equations hold for the unperturbed values of each quantity. The resulting system of differential equations can be solved by plugging in the ansatz that, for some real $\boldsymbol{k}$ and complex ω, all perturbations are proportional to $\exp[i(\boldsymbol{k}\cdot\boldsymbol{x}-\omega t)]$. This yields a linear system of equations in the perturbed quantities. Eliminating the perturbed quantities provides a relationship between $\boldsymbol{k}$, ω, and the unperturbed background.

In this work, we allow for an arbitrary number of ion fluids with arbitrary magnetization, and we include thermal terms. However, we still make some further assumptions to simplify the algebra. In particular, we assume there is only one neutral fluid, n, which does not respond to any perturbations; neglect collisional effects between nonneutral fluids ("Coulomb collisions"); and assume all other collision frequencies are constant. We also assume the perturbation is electrostatic; i.e., the magnetic field's response to the perturbation is negligible. Finally, we consider only those solutions where the wavevector $\boldsymbol{k}$ is perpendicular to the magnetic field $\boldsymbol{B}$. After considerable algebra, we find that the dispersion relation is

$$1 + \sum_{s\in\mathrm{ions}}\left(\frac{\lambda_{D,e}^2}{\lambda_{D,s}^2}\right)\frac{\mathcal{F}_s}{\mathcal{F}_e} = 0, \tag{A1a}$$

where the terms are defined as follows:

$$\mathcal{F}_s = \mathcal{A}_s\left(1 - \left[1 + \frac{2}{3\mu_s}\right]\mathcal{A}_s - \frac{\mathcal{B}_s}{\mu_s}\right)^{-1}, \tag{A1b}$$

$$\mathcal{A}_s = -i\frac{T_s^{(0)}}{m_s}\frac{\boldsymbol{k}\cdot\boldsymbol{k}}{\nu_{sn}\omega_s}\left[\frac{\mathcal{W}_s}{\mathcal{W}_s^2 + \kappa_s^2}\right], \tag{A1c}$$

$$\mathcal{B}_s = \frac{4m_n}{3(m_n + m_s)}\frac{(\boldsymbol{u}_s^{(0)} - \boldsymbol{u}_n)}{\omega_s}$$

$$\times \cdot\left(\left[\frac{\mathcal{W}_s}{\mathcal{W}_s^2 + \kappa_s^2}\right]\boldsymbol{k} + \left[\frac{\kappa_s}{\mathcal{W}_s^2 + \kappa_s^2}\right]\frac{\boldsymbol{k}\times\boldsymbol{B}}{|\boldsymbol{B}|}\right), \tag{A1d}$$

$$\mu_s = 1 + 2i\left(\frac{m_s}{m_n + m_s}\right)\frac{\nu_{sn}}{\omega_s}, \tag{A1e}$$

$$\mathcal{W}_s = 1 - i\omega_s/\nu_{sn}, \tag{A1f}$$

$$\omega_s = \omega - \boldsymbol{k}\cdot\boldsymbol{u}_s^{(0)}, \tag{A1g}$$

and the Debye length and magnetization parameter are defined in the usual way:

$$\lambda_{D,s}^2 = \frac{\epsilon_0 T_s^{(0)}}{q_s^2 n_s^{(0)}}, \qquad \kappa_s = \frac{q_s|\boldsymbol{B}|}{m_s\nu_{sn}}. \tag{A1h}$$

Above, $n_s^{(0)}$, $\boldsymbol{u}_s^{(0)}$, and $T_s^{(0)}$ are the background number density, velocity, and temperature (in energy units) of a nonneutral fluid s. By our assumptions, the neutral fluid does not respond to the perturbation, so the neutral velocity $\boldsymbol{u}_n$ is constant. Note that these expressions adopt the convention $q_e < 0$.

Through further manipulation, the dispersion relation may be rewritten into a ratio of polynomials in ω. We use the author's algebraic manipulation package, SymSolver,[6] to accomplish this task, rather than do it by hand. Considering only two ion species, as was done in this work, the resulting polynomials are 18th order in ω. Such a system is too complicated to solve analytically. However, there are many existing routines for finding the roots of polynomials numerically. In this work, we use the roots method from the numpy.polynomial package to find the roots of polynomials numerically for a given set of physical parameters and each value of $\boldsymbol{k}$.

A more detailed derivation and analysis for the TFBI theory can be found in Dimant et al. (2022). Note that there are a couple differences between the dispersion relation here and in that work. Here we account for the contribution from a potentially nonzero neutral velocity, even though all dispersion relation calculations discussed in this work occur at $\boldsymbol{u}_n = 0$. We include this contribution for future reference to allow for dispersion relation calculations outside the neutral frame. The other difference is an additional term that appears on the right-hand side of the generic dispersion relation in Dimant et al. (2022); this term comes from using the Poisson equation instead of quasi-neutrality. For the parameters of the simulation in our work, we confirmed numerically that this additional term has a negligible effect on growth rate predictions.

Appendix B
Numerical Scheme: Artificial Diffusion

The artificial hyperdiffusion terms in Ebysus primarily diffuse sharp fluctuations at small scales (five grid cells or less). These terms are similar to those in Bifrost (Gudiksen et al. 2011) but have been adapted to the multifluid simulations discussed in this work. In particular, these terms are added to the continuity, momentum (each component treated
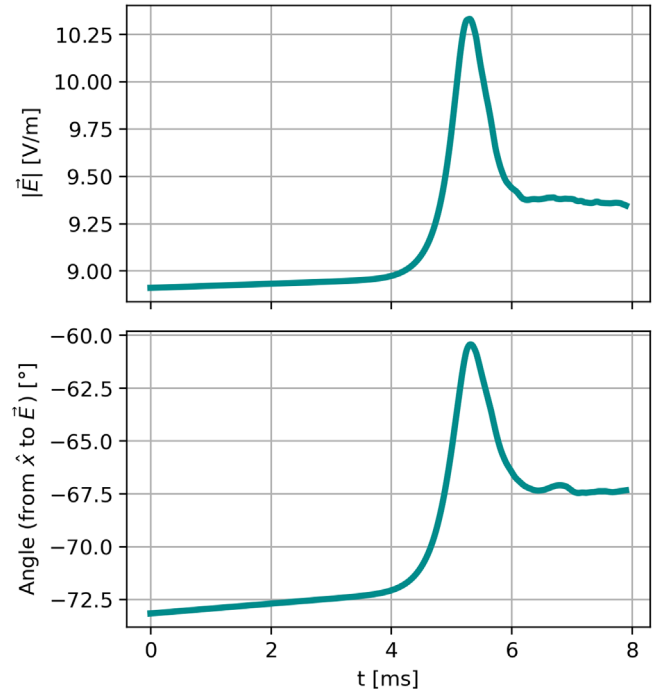
Figure 9. Mean electric field throughout the simulation of the TFBI. The top plot indicates the magnitude, while the bottom plot indicates the angle with respect to the positive x-axis.

separately), and energy Equations (1a), (1b), and (1c) for every fluid. Each of these equations, which can be expressed as $\partial f_s/\partial t = $ (original RHS), where $f_s = n_s$, $u_{x,s}$, $u_{y,s}$, $u_{z,s}$, or T_s becomes, after incorporating the hyperdiffusive terms,

$$\frac{\partial f_s}{\partial t} = (\text{original RHS}) + \nu_1 C_s^{(\text{fast})}$$

$$\times \sum_{x_i'\in\{x',y'\}}\frac{\partial}{\partial x_i'}\left[\frac{\partial f_s}{\partial x_i'}Q_{x_i'}\left(\frac{\partial f_s}{\partial x_i'}\right)\right], \tag{B1a}$$

where

$$Q_{x_i'}(g) = \left(\frac{\partial}{\partial x_i'}\frac{\partial g}{\partial x_i'}\right)\Big/\left(|g| + \frac{1}{q}\frac{\partial}{\partial x_i'}\frac{\partial g}{\partial x_i'}\right). \tag{B1b}$$

Here $\nu_1 = 0.01$ and $q = 1.0$ are constants that control the strength of the hyperdiffusion, $C_s^{(\text{fast})} = \sqrt{(\gamma T_s/m_s)^2 + B^2/(\mu_0 m_s n_s)}$ is the speed of the fast magnetosonic wave for fluid s, $\gamma = 5/3$ is the adiabatic index, and x' and y' are the spatial coordinates x and y normalized such that the grid cells each have a length of 1.

Appendix C
Simulation Electric Field

The electric field varies throughout the Ebysus simulations discussed in this work. Figure 9 plots the mean electric field for the main simulation of the TFBI presented in this work; see, for example, Section 3.2 and Figure 4. This figure shows the magnitude and direction of the mean electric field throughout the simulation, calculated by solving the electron momentum equation for $\boldsymbol{E}$ assuming no electron inertia. The magnitude increases roughly linearly from 8.91 to 8.97 V m^{-1} during the first 4.0 ms of the simulation, increases to its peak of 10.33 V m^{-1} at $t = 5.30$ ms, decreases, and then fluctuates

Evans et al.

before reaching its final value of 9.35 V m^{-1} at the end of the simulation. The angle increases roughly linearly from $-73°.2$ to $-72°.1$ during the first 4.0 ms, increases to its peak of $-60°.4$ at $t = 5.32$ ms, decreases, and then fluctuates before reaching its final value of $-67°.3$.

ORCID iDs

Samuel Evans ⓘ https://orcid.org/0000-0002-1127-7350
Meers Oppenheim ⓘ https://orcid.org/0000-0002-8581-6177
Juan Martínez-Sykora ⓘ https://orcid.org/0000-0002-0333-5717
Yakov Dimant ⓘ https://orcid.org/0000-0002-3807-5820

References

Abbett, W. P. 2007, ApJ, 665, 1469
Asplund, M., Grevesse, N., Sauval, A. J., & Scott, P. 2009, ARA&A, 47, 481
Ballester, J. L., Alexeev, I., Collados, M., et al. 2018, SSRv, 214, 58
Carlsson, M. 2007, in ASP Conf. Ser. 368, The Physics of Chromospheric Plasmas, ed. P. Heinzel, I. Dorotovič, & R. J. Rutten (San Francisco, CA: ASP), 49
Carlsson, M., De Pontieu, B., & Hansteen, V. H. 2019, ARA&A, 57, 189
Carlsson, M., & Stein, R. F. 1992, ApJL, 397, L59
Carlsson, M., & Stein, R. F. 1995, ApJL, 440, L29
Carlsson, M., & Stein, R. F. 2002, ApJ, 572, 626
Cheung, M. C. M., & Isobe, H. 2014, LRSP, 11, 3
Chintzoglou, G., De Pontieu, B., Martínez-Sykora, J., et al. 2021, ApJ, 906, 82
da Silva Santos, J. M., de la Cruz Rodríguez, J., Leenaarts, J., et al. 2020, A&A, 634, A56
De Pontieu, B., Title, A. M., Lemen, J. R., et al. 2014, SoPh, 289, 2733
Dimant, Y. S., & Oppenheim, M. M. 2004, JASTP, 66, 1639
Dimant, Y. S., Oppenheim, M. M., Evans, S., & Martinez-Sykora, J. 2022, arXiv:2211.05264
Dimant, Y. S., Oppenheim, M. M., & Fletcher, A. C. 2016, PhPl, 23, 084503
Dimant, Y. S., & Sudan, R. N. 1995, JGR, 100, 14605
Fletcher, A. C., Dimant, Y. S., Oppenheim, M. M., & Fontenla, J. M. 2018, ApJ, 857, 129
Fontenla, J. M. 2005, A&A, 442, 1099
Fontenla, J. M., Curdt, W., Haberreiter, M., Harder, J., & Tian, H. 2009, ApJ, 707, 482
Fontenla, J. M., Peterson, W. K., & Harder, J. 2008, A&A, 480, 839
Golding, T. P., Carlsson, M., & Leenaarts, J. 2014, ApJ, 784, 30
Golding, T. P., Leenaarts, J., & Carlsson, M. 2016, ApJ, 817, 125
Gudiksen, B. V., Carlsson, M., Hansteen, V. H., et al. 2011, A&A, 531, A154
Hansteen, V. H., de Pontieu, B., Carlsson, M., et al. 2007, PASJ, 59, S699
Hansteen, V. H., Martinez-Sykora, J., Carlsson, M., et al. 2023, ApJ, 944, 131
Hyman, J. M. 1979, in Advances in Computer Methods for Partial Differential Equations—III (New Brunswick, NJ: International Association for Mathematics and Computers in Simulation), 313
Ishikawa, R., Trujillo Bueno, J., del Pino Alemán, T., et al. 2021, SciA, 7, eabe8406
Kagan, L. M., & Maurice, J. P. 2004, JGRA, 109, A12302
Leake, J. E., DeVore, C. R., Thayer, J. P., et al. 2014, SSRv, 184, 107
Leenaarts, J., Carlsson, M., Hansteen, V., & Rutten, R. J. 2007, A&A, 473, 625
Madsen, C. A., Dimant, Y. S., Oppenheim, M. M., & Fontenla, J. M. 2014, ApJ, 783, 128
Martínez-Sykora, J., de la Cruz Rodríguez, J., Gošić, M., et al. 2023, ApJL, 943, L14
Martínez-Sykora, J., De Pontieu, B., & Hansteen, V. 2012, ApJ, 753, 161
Martínez-Sykora, J., De Pontieu, B., Hansteen, V., & Carlsson, M. 2015, RSPTA, 373, 20140268
Martínez-Sykora, J., De Pontieu, B., Hansteen, V. H., et al. 2017, Sci, 356, 1269
Martínez-Sykora, J., Szydlarski, M., Hansteen, V. H., & De Pontieu, B. 2020, ApJ, 900, 101
Nóbrega-Siverio, D., Martínez-Sykora, J., Moreno-Insertis, F., & Carlsson, M. 2020, A&A, 638, A79
Oppenheim, M., Dimant, Y., Longley, W., & Fletcher, A. C. 2020, ApJL, 891, L9
Pereira, T. M. D., De Pontieu, B., & Carlsson, M. 2013, ApJ, 764, 69
Przybylski, D., Cameron, R., Solanki, S. K., et al. 2022, A&A, 664, A91
Trujillo Bueno, J., Asensio Ramos, A., & Shchukina, N. 2006, in ASP Conf. Ser. 358, Solar Polarization 4, ed. R. Casini & B. W. Lites (San Francisco, CA: ASP), 269
Wargnier, Q. M., Martínez-Sykora, J., Hansteen, V. H., & De Pontieu, B. 2022, ApJ, 933, 205
Wedemeyer, S., Freytag, B., Steffen, M., Ludwig, H. G., & Holweger, H. 2004, A&A, 414, 1121